

H α Kinematics of the SINGS Nearby Galaxies Survey. I^{*}

O. Daigle^{1,5†}, C. Carignan^{1,5}, P. Amram^{2,5}, O. Hernandez^{1,2,5}, L. Chemin¹,
C. Balkowski^{3,5} and R. Kennicutt⁴

¹*Observatoire du mont Mégantic, LAE, Université de Montréal, C. P. 6128 succ. centre ville, Montréal, Québec, Canada H3C 3J7.*

²*Observatoire Astronomique de Marseille Provence, Laboratoire d'Astrophysique de Marseille, 2 place Le Verrier, F-13248 Marseille Cedex 04, France.*

³*Observatoire de Paris, section Meudon, GEPI, CNRS UMR 8111 et Université Paris 7, 5 place J. Janssen, 92195 Meudon Cedex, France.*

⁴*Department of Astronomy, Steward Observatory, 933 N. Cherry Ave., Tucson, AZ 85721-0065, USA.*

⁵*Visiting Astronomer, Canada–France–Hawaii Telescope, operated by the National Research Council of Canada, the Centre National de la Recherche Scientifique de France, and the University of Hawaii.*

Accepted . Received ; in original form

ABSTRACT

This is the first part of an H α kinematics follow-up survey of the SINGS sample. The data for 28 galaxies are presented. The observations were done on three different telescopes with FANTOMM, an integral field photon counting spectrometer, installed in the respective focal reducer of each telescope. The data reduction was done through a newly built pipeline with the aim of producing the most homogenous data set possible. Adaptive spatial binning was applied to the data cubes in order to get a constant signal-to-noise ratio across the field of view. Radial velocity and monochromatic maps were generated using a new algorithm and the kinematical parameters were derived using tilted-ring models.

Key words: galaxies: kinematics and dynamics – methods: observational. – techniques: radial velocities.

1 INTRODUCTION

The Legacy survey SINGS (Spitzer Infrared Nearby Galaxies Survey) wants to characterise the infrared emission across the entire range of galaxy properties and star formation environments, including regions that until now have been inaccessible at infrared wavelengths (Kennicutt et al., 2003). SINGS will provide:

- new insights into the physical processes connecting star formation to the ISM properties of galaxies;
- a vital foundation of data, diagnostic tools, and astrophysical inputs for understanding SPITZER observations of the distant universe and ultraluminous and active galaxies;
- an archive that integrates visible/UV and IR/submillimeter studies into a coherent self-consistent

whole, and enables many follow-up investigations of star formation and of the ISM.

The SPITZER observations will provide images in 7 different bands from 3.6 μ m to 160 μ m and spectroscopic data at medium and low resolution in the range 5–95 μ m. These data will be used to trace the distribution and content of different dust components, from the PAHs and very small grains in the mid-IR, to the big grains in the far-IR (del Burgo et al. 2003, Kennicutt et al. 2003). Ancillary multiwavelength observations will provide images in X-rays, UV (1300–2800 Å imaging and spectrophotometry), BVRIJHK, H α , Pa α , FIR, submillimeter, CO and H_I. A total of 20 ground- and space-based telescopes are providing supporting data.

These data will help understand the process of star formation and feedback mechanisms that are fundamental parameters regulating the formation and evolution of galaxies. History of star formation has been strongly different for galaxies of different morphological type and luminosity. While short events of star formation, probably triggered by violent merging, formed most stars in elliptical galaxies, late-

* Based on observations collected at the European Southern Observatory, La Silla, Chile.

† E-mail: odaigle@astro.umontreal.ca

type systems seem to have their star formation modulated by the angular momentum (Sandage, 1986) or by the mass of the initial system (Boselli, 2001). The process of star formation and feedback must thus be clearly understood in order to understand galaxies' evolution. However, these physical processes are still poorly known. The primordial atomic gas has to condense into molecular clouds to form stars. The newly formed stars inject metals into the interstellar medium via stellar winds, heat the dust and ionise the surrounding gas. It seems that the activity of star formation is regulated by the total gas surface density (Kennicutt, 1989), but it is still unclear what is the role of rotation in this process.

Even as important as it seems, no gathering of optical kinematical data was planned for the SINGS galaxies. This paper, by providing the $H\alpha$ kinematics over the whole optical extent for 28 galaxies of the SINGS sample, wants to make up for this lack. A total of 58 SINGS galaxies are potentially observable in the $H\alpha$ emission line (see section 2.1). The $H\alpha$ kinematics of the 30 remaining galaxies of the observable part of the sample will be published in a forthcoming paper. These data were obtained with FANTOMM on three different telescopes (see section 2.3). FANTOMM is an integral field spectrometer made of a photon-counting camera using a third generation photo-cathode, a scanning Fabry-Perot (FP) and a narrow-band interference filter. FANTOMM was coupled to the focal reducer of the telescopes used. The photo-cathode used has a high quantum efficiency ($\sim 30\%$ at $H\alpha$). This camera enables one to scan rapidly (~ 5 – 10 minutes) the FP Free Spectral Range (FSR) and to cycle many times during an observation, thus averaging changing photometrical conditions, as compared to CCD observations where scanning must be done slowly to overcome the readout noise (details about the camera can be found in Hernandez et al., 2003 and Gach et al., 2002). In this paper, section 2 gives an overview of the observational campaign and of the galaxies studied. Section 3 discusses how the data were reduced, processed and how the kinematical data and parameters were extracted. Section 4 provides all the maps extracted from the work done in section 3. Section 5 discusses the advantages of FP kinematical data as compared to other kinematical data. A short appendix is added to comment the observational characteristics of the galaxies presented. Once completed, the data set will be available in the SINGS database, as for the other SINGS ancillary surveys.

2 OBSERVATIONS

2.1 The sample

The SINGS sample as defined by Kennicutt et al. (2003) is composed of 75 nearby ($\Delta < 30$ Mpc, median of 9.5 Mpc, for $H_0 = 70 \text{ km s}^{-1} \text{ Mpc}^{-1}$) galaxies, covering a wide range in a 3D parameter space of physical properties:

- morphological type (E to Im), which is also correlated with the Star Formation Rate (SFR) per unit mass, gas fraction and bulge/disk ratio;

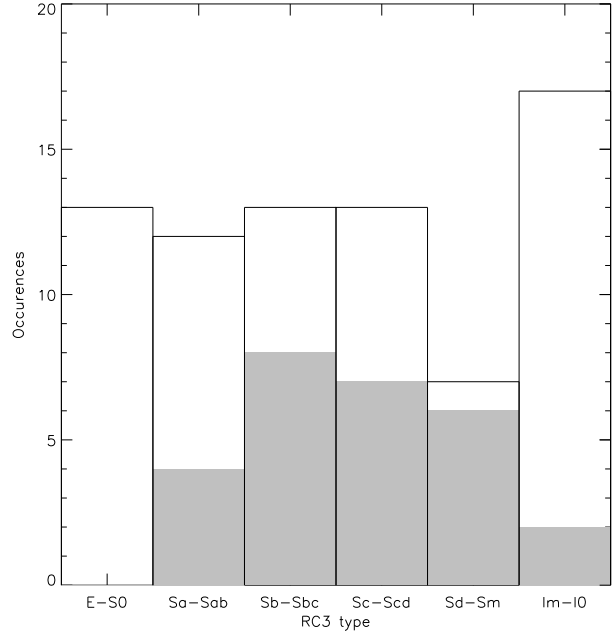


Figure 1. The SINGS RC3 galaxy type distribution. The grey area shows the galaxies presented in this paper.

- luminosity (IR-quietest to luminous IR galaxies), which is also correlated with galaxy mass, internal velocity and mean metallicity;
- FIR/optical ratio covering over 3 orders of magnitude, which is also correlated with dust optical depth, dust temperature and inclination.

Roughly twelve galaxies were chosen in each RC3 type (E–S0, Sa–Sab, Sb–Sbc, Sc–Scd, Sd–Sm and Im–I0) which allows the coverage of a full combination of luminosity and infrared/optical ratio ($5 \times 10^5 L_\odot < L_V < 2 \times 10^{11} L_\odot$, $10^7 L_\odot < L(IR) < 10^{11} L_\odot$ and $0.02 < L(IR)/L_R < 42$). Care was also taken to choose galaxies covering a wide range of other properties, such as nuclear activity, inclination, surface brightness, CO/ H_I ratio, bar structure, spiral arm structure, isolated/interacting, group members, cluster members. Galaxies lying far from the Galactic plane were preferred to avoid a high density of foreground stars and galactic extinction.

From the 75 galaxies of the sample, only those which present H_{II} regions (star formation regions) can be observed in $H\alpha$ in order to map their kinematics. Mainly, most early type galaxies (E to S0–Sa) lack $H\alpha$ emission and could not be observed. Starting from Sb galaxies, it is usually possible to extract the $H\alpha$ kinematics. Figure 1 shows the morphological type distribution of the presented galaxies and highlights the observational bias caused by the lack of $H\alpha$ emission in early-type galaxies. Also, Im–I0 galaxies are usually very small and could not be observed on the 1.6-m telescope at the Observatoire du mont Mégantic. These galaxies need a 4 meters class telescope to be observed. The velocity maps

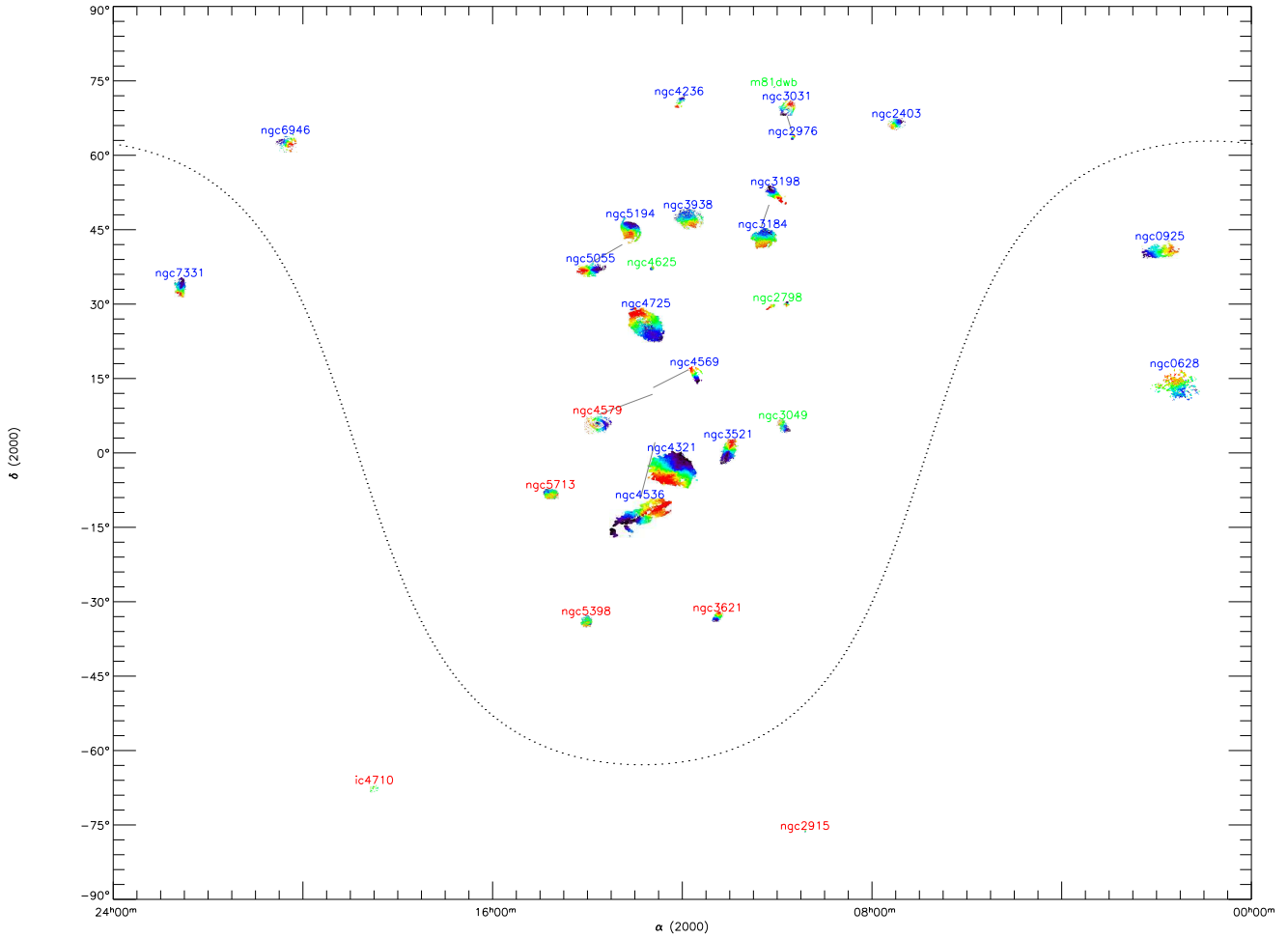


Figure 2. The SINGS $H\alpha$ kinematics sky coverage so far. The names in blue correspond to the observations done at the OMM, in green at the CFHT and in red at the ESO 3.6m telescope. Galaxies relative sizes are to scale. The galactic equator is shown as the dotted line. Naturally, there is a strong concentration toward the Virgo cluster.

and the observed galaxies' positions are shown in Figure 2. This Figure also shows the relative sizes of the galaxies (in kpc). The basic galaxy parameters are presented in Table 1. Table 2 gives the observation conditions and information for each galaxy.

2.2 The hardware

All the observations were made with the integral field spectrometer, **FANTOMM**. It consists of a narrow-band (typically 15\AA) interference filter, a FP interferometer and a photon counting camera, used as the imaging device. **FANTOMM** is coupled to the respective focal reducer of the telescopes onto which it is attached. The focal reducer **PANORAMIX** is used at the 1.6-m telescope of the Observatoire du mont Mégantic (OMM), **CIGALE** at the ESO (La Silla) 3.6-m telescope and **MOS/FP** at the CFH 3.6-m telescope. The effective focal ratio, pixel size and field of view are summarised in table 3. Interestingly, the pixel size obtained at the OMM ($1.6''$),

where most of the galaxies were observed, is a close match to the one achieved by the SPITZER's Infrared Array Camera (better than $2''$ in the $3.6\text{--}8\mu\text{m}$ range). This is, however, pure coincidence.

The interference filter is used to “select” the radial velocity range that will be observed. It is chosen to allow only the galaxy's $H\alpha$ emission to pass through. Since most galaxies radial velocities span a maximum of $\pm 250 \sin i \text{ km s}^{-1}$, a maximum Doppler shift of $\pm 5.5\text{\AA}$ is expected around the galaxy's redshifted emission. The interference filter used must allow this emission to pass through whilst being as narrow as possible to avoid too much sky background emission from reaching the detector. A collection of 23 filters having a FWHM of $\sim 15\text{\AA}$, covering the red spectrum from 6565\AA to 6785\AA in steps of 10\AA was used to observe the galaxies in the sample. This set of filters allows galaxies with $-300 \text{ km s}^{-1} \lesssim v_{sys} \lesssim 10000 \text{ km s}^{-1}$ to be observed. Figure 3 shows a typical filter used for the observations. Centered at $\sim 6598\text{\AA}$, it has a FWHM of 18\AA . By tilting the filter by a

Table 1. Observational data for the SINGS H α kinematics sample.

Galaxy Name	α (J2000) (hh mm ss)	δ (J2000) ($^{\circ}$ ' ")	Type RC3	Δ ⁽¹⁾ (Mpc)	$D_{25}^{b,i}$ ⁽²⁾ ($''$)	$B_T^{b,i}$ ⁽³⁾	$M_B^{b,i}$ ⁽⁴⁾	Systemic Velocity ⁽⁵⁾ (km s $^{-1}$)
NGC 628	01 36 41.8	+15 47 00	SA(s)c	11.4	10.5 x 9.5	9.95	−20.33	657
NGC 925	02 27 16.8	+33 34 41	SAB(s)d	9.3	11.2	10.6	−19.24	554
NGC 2403	07 36 54.5	+65 35 58	SAB(s)cd	4.2	21.4	8.5	−19.61	132
NGC 2798	09 17 22.9	+41 59 59	SB(s)a pec	24.7	2.6 x 1	13.04	−18.92	1726
NGC 2915	09 26 11.5	−76 37 35	I0	2.7	1.9 x 1	13.25	−13.91	468
NGC 2976	09 47 15.4	+67 54 59	SAc pec	3.5	5.9 x 2.7	10.82	−16.90	3
NGC 3049	09 54 49.6	+09 16 18	SB(rs)ab	19.6	2.2 x 1.4	13.04	−18.42	1494
NGC 3031	09 55 33.2	+69 03 55	SA(s)ab	3.5	26.9 x 14.1	7.89	−19.83	−34
UGC 5423	10 05 30.6	+70 21 52	Im	3.5	0.9 x 0.6	15.19	−12.53	350
NGC 3184	10 18 17.0	+41 25 28	SAB(rs)cd	8.6	7.4 x 6.9	10.36	−19.31	592
NGC 3198	10 19 54.9	+45 33 09	SB(rs)c	14.5	7.8	11.1	−19.70	660
NGC 3521	11 05 48.6	−00 02 09	SAB(rs)bc	9	11 x 5.1	9.83	−19.94	805
NGC 3621	11 18 16.3	−32 48 45	SA(s)d	6.2	12.3 x 7.1	10.28	−18.68	727
NGC 3938	11 52 49.4	+44 07 15	SA(s)c	12.2	5.4 x 4.9	10.90	−19.53	809
NGC 4236	12 16 42.1	+69 27 45	SB(s)dm	2.2	16.4	9.5	−17.21	2
NGC 4321	12 22 55.2	+15 49 23	SAB(s)b	16.1	7.4	10.0	−21.03	1590
NGC 4536	12 34 27.1	+02 11 16	SAB(rs)bc	25	7.6 x 3.2	11.16	−20.82	1808
NGC 4569	12 36 49.8	+13 09 46	SAB(rs)ab	20	9.5 x 4.0	10.26	−21.24	−235
NGC 4579	12 37 43.6	+11 49 05	SAB(rs)b	20	5.9 x 4.7	10.48	−21.18	1591
NGC 4625	12 41 52.7	+41 16 25	SAB(rs)m pec	9.5	2.2 x 1.9	12.92	−16.97	609
NGC 4725	12 50 26.6	+25 30 06	SAB(r)ab pec	17.1	10.7 x 7.6	10.11	−21.05	1206
NGC 5055	13 15 49.3	+42 01 45	SA(rs)bc	8.2	12.6 x 7.2	9.31	−20.26	504
NGC 5194	13 29 52.7	+47 11 43	SA(s)bc pec	8.2	11.2 x 6.9	8.96	−20.61	463
NGC 5398	14 01 21.5	−33 03 50	SB(rs)dm	15	2.8 x 1.7	12.78	−18.10	1216
NGC 5713	14 40 11.5	−00 17 21	SAB(rs)bc pec	26.6	2.8 x 2.5	11.84	−20.28	1883
IC 4710	18 28 38.0	−66 58 56	SB(s)m	8.5	3.6 x 2.8	12.5	−17.14	741
NGC 6946	20 34 52.0	+60 09 15	SAB(rs)cd	5.5	14.9	7.92	−20.78	46
NGC 7331	22 37 04.1	+34 24 56	SA(s)b	15.7	10.5 x 3.7	10.35	−20.63	816

⁽¹⁾ Δ : distance in Mpc, flow-corrected for $H_0=70$ km s $^{-1}$ Mpc $^{-1}$, as presented in Kennicutt et al. (2003).

⁽²⁾ $D_{25}^{b,i}$: optical diameter at the 25 magnitude/arcsecond 2 in B, corrected for the effects of projection and extinction. Taken from the RC3.

⁽³⁾ $B_T^{b,i}$: corrected total apparent magnitude in B. Taken from the RC3.

⁽⁴⁾ $M_B^{b,i}$: corrected total absolute magnitude in B. Calculated from Δ and $B_T^{b,i}$.

⁽⁵⁾ Systemic velocity : galaxy's systemic velocity. Taken from Kennicutt et al. (2003).

couple of degrees, it is possible to blue shift its central wavelength by a few Å to allow the filter to be exactly centered on the galaxy's rest H α emission. The filters must also be chosen according to the expected outdoor temperature as they are typically blue shifted as temperature goes down. This shift is of the order of $-0.2\text{Å}\cdot\text{K}^{-1}$. As filters age, they also tend to blue shift. They must be scanned regularly to keep a good knowledge of their characteristics.

The FP interferometer is chosen to allow most of the H α emission of the galaxy to be visible in a single Free Spectral Range (FSR). The interference orders of the FP interferometers used vary from $p=609$ ($\text{FSR} = 10.93\text{Å}$) to $p=899$ ($\text{FSR} = 7.3\text{Å}$) at rest H α . Another parameter that has to be taken into account is the FP *Finesse*. The Finesse, F , is a dimensionless value expressing the spectral resolution, R , of the etalon such as

$$R = \frac{F\lambda_0}{\text{FSR}} = \frac{\Delta\lambda}{\lambda}$$

and

$$\text{FSR} = \frac{\lambda_0}{p}.$$

To properly sample the light that comes out of the FP, the number of channels scanned must be at least 2.2 times (Nyquist) the Finesse. Many different factors affect the Finesse: the reflectivity of the reflecting plates of the FP, the optical and mechanical properties of the surfaces (usually polished to $< \frac{\lambda}{100}$), the temperature, the humidity, and the observational setup (the parallelism, the accuracy of the focus of the focal reducer). In fact, the environmental effects and the observational setup should not affect the Finesse, but, as shown by Table 4, the scatter in Finesses obtained must be explained by these phenomena. Finesses achieved for the observations presented in this paper range from 8 to 20. A total of 3 different FP etalons were used for the observations. The interference filter and PF interferometer

Table 2. Journal of the Fabry-Perot Observations.

Galaxy Name	Date	$\lambda_c^{(4)}$ (Å)	Filter FWHM ⁽⁵⁾ (Å)	$T_{max}^{(6)}$ (%)	Effective integration $t_{exp}^{(7)}$ (min.)	$t_{channel}^{(8)}$ (min)	$p^{(9)}$	Fabry-Perot FSR ⁽¹⁰⁾ (km s ⁻¹)	$F^{(11)}$	$R^{(12)}$	Sampling nch ⁽¹³⁾	stp ⁽¹⁴⁾ (Å)
NGC 628 ⁽¹⁾	18/11/2003	6598	18.2	73	149	2.33	899	333.47	23.6	21216	64	0.11
NGC 925 ⁽¹⁾	11/02/2002	6584	15	75	132	2.75	765	391.88	16	12240	48	0.18
NGC 2403 ⁽¹⁾	17/11/2002	6569	10	50	120	3.00	765	391.88	14	10710	40	0.21
NGC 2798 ⁽²⁾	04/04/2003	6608	16.2	69	96	2.00	899	333.47	16	14384	48	0.15
NGC 2915 ⁽³⁾	04/21/2004	6581	19.8	60	149	4.67	609	492.27	14.3	8580	32	0.34
NGC 2976 ⁽¹⁾	30/01/2003	6581	19.8	60	184	3.83	899	333.47	16.5	14834	48	0.15
NGC 3049 ⁽²⁾	08/04/2003	6598	18.2	73	144	3.00	899	333.47	17.4	15643	48	0.15
NGC 3031 ⁽¹⁾	06/02/2003	6581	19.8	60	272	5.55	899	333.47	14.3	12856	48	0.15
UGC 5423 ⁽²⁾	06/04/2003	6565	15	40	120	2.50	899	333.47	18.5	16632	48	0.15
NGC 3184 ⁽¹⁾	18/02/2004	6584	15.5	74	162	3.37	765	391.88	17.6	13464	48	0.18
NGC 3198 ⁽¹⁾	06/03/2003	6584	15.5	74	260	5.00	899	333.47	23	20976	52	0.14
NGC 3521 ⁽¹⁾	19/02/2004	6584	15.5	74	120	2.50	765	391.88	16.0	12240	48	0.18
NGC 3621 ⁽³⁾	04/20/2004	6584	15.5	74	128	4.00	609	492.27	14.4	8640	32	0.34
NGC 3938 ⁽¹⁾	11/03/2004	6584	15.5	74	128	2.66	765	391.88	16.8	12852	48	0.18
NGC 4236 ⁽¹⁾	27/02/2004	6581	19.8	60	182	3.50	899	333.47	23	20977	52	0.14
NGC 4321 ⁽¹⁾	25/02/2003	6608	16.2	69	260	5.00	899	333.47	23	20977	52	0.14
NGC 4536 ⁽¹⁾	14/03/2004	6598	18.2	73	163	3.40	765	391.88	21.3	16295	48	0.18
NGC 4569 ⁽¹⁾	11/03/2002	6569	15.0	60	152	3.80	765	391.88	20.5	15682	40	0.21
NGC 4579 ⁽¹⁾	04/04/2002	6598	10.0	60	92	2.30	609	492.27	19.6	14494	40	0.27
NGC 4625 ⁽²⁾	06/04/2003	6581	19.8	60	120	2.50	899	333.47	15.9	14294	48	0.15
NGC 4725 ⁽¹⁾	19/02/2004	6584	15.5	74	120	2.50	765	391.88	18.7	14305	48	0.18
NGC 5055 ⁽¹⁾	14/03/2004	6584	15.5	74	128	2.66	765	391.88	16.8	12852	48	0.18
NGC 5194 ⁽¹⁾	18/05/2003	6581	19.8	60	246	5.14	899	333.47	20.7	18609	48	0.15
NGC 5398 ⁽³⁾	04/10/2004	6598	18.2	73	149	4.66	609	492.27	12.0	7308	32	0.34
NGC 5713 ⁽³⁾	04/13/2004	6608	16.2	69	150	6.25	609	492.27	9.5	5785	24	0.45
IC 4710 ⁽³⁾	04/15/2004	6598	18.2	73	48	2.00	609	492.27	8.8	5359	24	0.45
NGC 6946 ⁽¹⁾	19/11/2002	6569	10	50	120	2.00	765	391.88	14	10710	40	0.21
NGC 7331 ⁽¹⁾	03/11/2002	6584	15.5	74	174	3.62	765	391.88	15.9	12164	48	0.18

⁽¹⁾ OMM : Observatoire du mont Mégantic, Québec, Canada. 1.6m telescope.

⁽²⁾ CFHT : Canada-France-Hawaii Telescope, Hawaii, USA. 3.6m telescope.

⁽³⁾ ESO : European Southern Observatory, La Silla, Chile, 3.6m telescope.

⁽⁴⁾ λ_c : non tilted filter central wavelength at 20°C.

⁽⁵⁾ FWHM : non tilted filter Full Width Half Maximum at 20°C.

⁽⁶⁾ T_{max} : non tilted filter maximum transmission at λ_c and at 20°C.

⁽⁷⁾ t_{exp} : total effective exposure time in minutes (Total exposure time * mean counting efficiency).

⁽⁸⁾ $t_{channel}$: total effective exposure time per channel in minutes (total exposure time per channel * mean counting efficiency).

⁽⁹⁾ p : FP interference order at H α .

⁽¹⁰⁾ FSR : FP Free Spectral Range at H α in km s⁻¹.

⁽¹¹⁾ F : mean Finesse through the field of view.

⁽¹²⁾ R : spectral resolution ($\Delta\lambda/\lambda$) according to the computed *Finesse*.

⁽¹³⁾ nch : number of channels done by cycle in multiplex observations.

⁽¹⁴⁾ stp : wavelength step in Å.

must be chosen so that no more than 3 FSRs of the etalon pass through the filter, as shown in figure 3.

The photon counting camera used for this survey is based on a GaAs Hamamatsu photocathode coupled with a Dalsa commercial CCD. The photocathode has a quantum efficiency of $\sim 28\%$ at H α and the CCD has 1024×1024 $12.5\mu\text{m}$ square pixels. The CCD was operated in its low spatial resolution mode, where pixels are binned 2×2 , and at a frame rate of 40 frames per seconds. The effective pixel sizes on the sky are given in Table 3. The photon count-

ing camera is an essential tool to achieve such a survey. Its ability to rapidly scan the FP interferometer allows the photometrical conditions' variations to be averaged out. For comparison, in CCD observations, each FP channel must be observed for at least 5 contiguous minutes to make sure that the read-out noise of the CCD does not mask the weak galaxy's signal. This means that photometrical conditions must not significantly change for ~ 4 hours with CCD observations (given that 48 FP channels are scanned). In photon counting, channels are observed for 5 to 15 seconds and

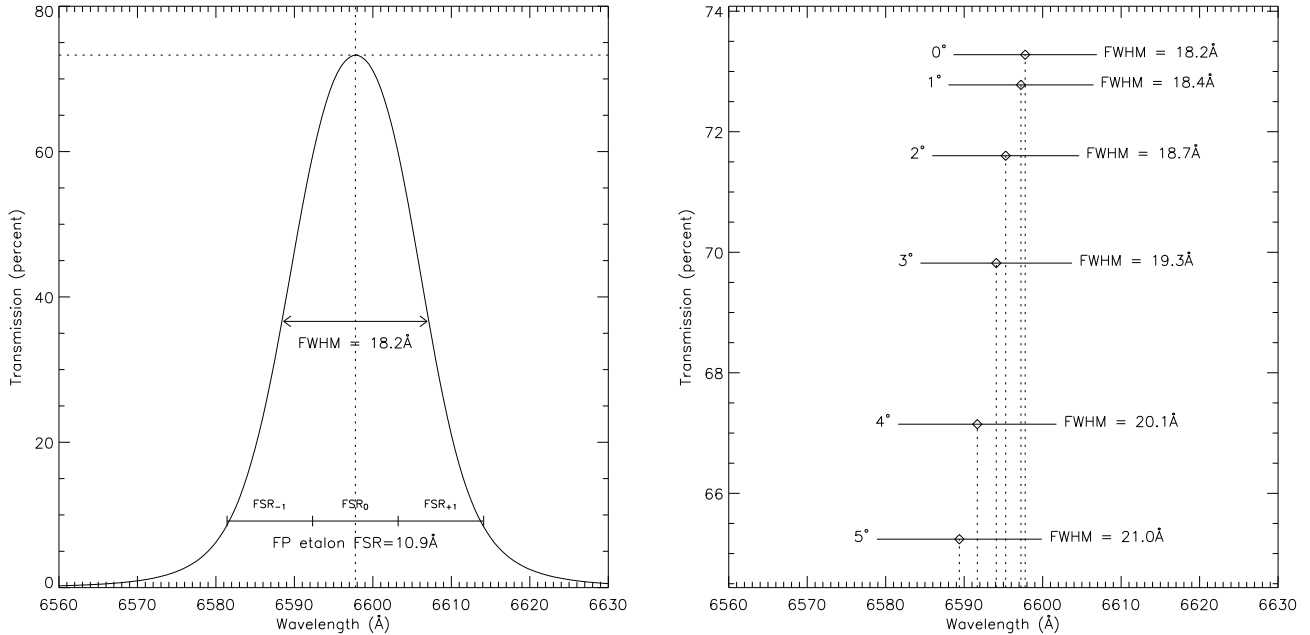


Figure 3. Left panel shows a typical interference filter transmission curve (experimental data) at 20°C. As shown in the right panel, filters may be tilted by a few degrees to blue shift the peak transmission wavelength by a couple of Å to allow it to be centered on the H α emission of a galaxy, at the price of a broadened transmission curve and a decreased peak transmission. In the bottom of the left panel is shown how FP interferometer and interference filters must be chosen to avoid having too many Free Spectral Ranges to pass through the filter.

cycles are looped every 4 to 15 minutes. Many cycles are made during an observation. Signal-to-noise ratio (SNR) estimations can be made throughout the observations and the observer can decide when to stop the integration. Since the calibration lamp is pretty strong as compared to galaxies' fluxes, the calibrations are done in analog mode (non photon counting). Typically, calibration channels are integrated 1 second each.

2.3 Observing runs

The observations of the sample presented here were spread over ten observing runs taking place in the last two years. Eight runs took place at the Observatoire du mont Megantic 1.6-m telescope (OMM), where FANTOMM is a permanent instrument. FANTOMM was taken to the Canada-France-Hawaii 3.6-m Telescope (CFHT) and the European Southern Observatory 3.6-m telescope (ESO/La Silla) as a visitor instrument for the other two runs of this survey. The large field of view available at the OMM permitted the observation of large galaxies (NGC 5194, NGC 3031...) in one single field. Smaller galaxies visible in the northern hemisphere were observed at the CFHT. A single observing run took place in the southern hemisphere on the ESO/La Silla telescope in April 2004. Few galaxies of the SINGS survey were visible at that time, resulting in a poor coverage of galaxies at negative declinations.

3 DATA REDUCTION

Raw observational data consist of many data files that contain photons' positions for every cycle/channel duo. If cycling is done with, say, 15 seconds per channel integration time, one file is created every 15 seconds. Data reduction consists of the following steps:

- integration of the raw data files into an interferogram data cube (3D data cube sliced for every FP channel);
- phase correction of the interferograms to create wavelength-sorted data cubes (3D data cube sliced for every wavelength interval);
 - hanning spectral smoothing;
 - sky emission removal;
 - spatial binning/smoothing;
- extraction of radial velocity maps from emission line positions;
 - addition of the astrometric information (World Coordinate System information) to the data files;
 - kinematical information extraction.

All the reduction was performed with IDL routines inspired by the ADHOCw reduction package (<http://www-obs.cnrs-mrs.fr/adhoc/adhoc.html>), except for the last two steps, in which cases third party software was used (see respective sections for more details). The IDL reduction package was written to allow more flexibility of the data reduction, such as telescope guiding error correction, better removal of the sky background

Table 3. FANTOMM characteristics on various telescopes.

Telescope Name	D m ⁽¹⁾	F/D ⁽²⁾	Pixel size (") ⁽³⁾	FOV (') ⁽⁴⁾	FOV _{unvign} (') ⁽⁵⁾
CFHT	3.6	2.96	0.48	5.83	3.91
ESO	3.6	3.44	0.42	5.01	5.01
OMM	1.6	2.00	1.61	19.43	19.43

⁽¹⁾D : telescope diameter in meter.

⁽²⁾F/D : focal length over telescope diameter ratio calculated from the effective pixel size on the sky.

⁽³⁾Pixel size : pixel size after binning 2×2, the original GaAs system providing 1024×1024 pixels of 12.5 μ m.

⁽⁴⁾FOV : diagonal Field Of View of the detector.

⁽⁵⁾FOV_{unvign} : unvignetted (usable) field of view.

emission through sky cube fitting, stronger emission line barycenter determination algorithm, etc. The newly introduced reduction routines are summarized here. More information on this reduction package will be available in a forthcoming paper (Daigle et al. 2006).

3.1 Raw data integration and wavelength map creation

Files stored during an observation are made of the position of every photon that fell on the detector for a given FP position. The observed wavelength through a FP etalon is given by

$$p\lambda = 2ne \cos \theta,$$

where p is the interference order at λ_0 (H α or 6562.78Å for all observations presented in this paper), n the index of the medium, e the distance between the plates of the FP and θ the incidence angle on the FP. For a given gap e and index n , every θ in a single channel is exposed to a different wavelength, which is to say that different pixels see different wavelengths. Thus, a phase calibration must be applied to transform raw interferograms into wavelength-sorted data cubes. This calibration is obtained by scanning a narrow Ne emission line. The bright line at 6598.95Å has been chosen since it falls close to the red-shifted H α emission lines observed, limiting the phase shift in the dielectric layer of the FP. This calibration must be done in exactly the same conditions as the observations. It is thus convenient to acquire this calibration data just before starting an integration, when the telescope is already on the object. Since these calibrations are done with the camera in analog mode (as compared to photon counting mode), the overhead is very small (of the order of a minute). This allows one to perform a calibration at the beginning and at the end of an integration and to sum them in order to average tiny variations of the FP etalon during the integration.

From this calibration data, a phase map is created. The phase map provides the shift that has to be applied in the spectral dimension to every pixel of the interferogram

cube to bring all channels to the same wavelength. By applying this phase map to the interferogram data cube, the wavelength-sorted data cube is created. An uncertainty still remains on the zero point of the velocity scale since the observed wavelength is only known modulo the FSR of the interferometer

$$FSR \equiv \Delta\lambda = \frac{\lambda_0}{p}.$$

This uncertainty is removed by means of comparisons with long-slit spectroscopy or 21-cm H $_I$ data.

The computed wavelength of every slice of the resulting (calibrated) data cube is not absolute. When the observed wavelength is far from the calibration wavelength, the difference will increase. This is caused mainly by the semi reflective, high Finesse coating of the FP etalon, which is hard to model. Absolute calibrations (in development), done at the same scanning wavelength would be a way of getting rid of these differences. Absolute post-calibration using observed sky spectrum emission lines in the data cube, which must include compensation for the interference filter transmission curve, has been worked on but requires more testing to prove its accuracy. Nevertheless, *relative* wavelength measurements are accurate to a fraction of a channel ($< 0.05\text{\AA}$) over the field. This leads to line of sight velocity (LOSv) measurement errors of less than 3 km s^{-1} .

Since the observational data are split in files representing a maximum of 15 seconds integration, it is possible to correct slight telescope guiding errors that could occur throughout the entire integration (typically 2–3 hours). This correction must be made at the same time as the raw data integration. But, as a spatial translation in the interferogram domain will induce a wavelength shift in the spectral domain, the phase calibration must be applied at the same time as the raw integration. Results presented in this paper have undergone the phase calibration at the same time as the raw data integration in order to render guiding error corrections possible.

3.2 Sky emission removal

The sky emission in the neighborhood of H α at rest, caused by geocoronal OH molecules is often stronger than the galaxy's diffuse H α emission. It is thus highly important to properly remove this emission prior to the extraction of the radial velocity map. As opposed to the ADHOCw package, where the OH emission lines are removed by the subtraction of a single integrated profile taken from user-selected sky regions, the data presented in this paper have been processed differently. Due to inhomogeneities in the spatial and spectral responses of the interference filter, the subtraction of a single spectrum can lead to positive and negative residuals in the data cube, where not enough or too much of the spectrum were subtracted. To avoid having to deal with such issues, and to improve the galaxies' signal coverage, a sky cube has been reconstructed by taking single pixel's spectra in the sky dominated regions and interpolating (or extrapolating) it in the galaxy's dominated spectra. This sky cube was then subtracted from the data cube. This proved to be a

Table 4. FP interferometers characteristics

Interferometer	p	FSR	F	R
1	899	333.47	15.6 – 23.6	14294 – 21216
2	765	391.88	14.0 – 21.3	10710 – 16295
3	609	492.27	8.8 – 19.6	5259 – 14494

much better procedure. For best results, the surface covered by the sky dominated regions and the galaxy dominated regions should be in a $\sim 1:1$ ratio.

3.3 Adaptive spatial binning and smoothing

In order to allow the LOSV of a galaxy's region to be properly determined, a minimum SNR is required. Cappellari & Copin (2003) used 2D Voronoi tessellations to create uniform SNR velocity maps of Sauron data. Starting from this work, an adaptive binning algorithm was developed for FP 3D data cubes. The main difference between the two algorithms is the way by which pixels are accreted into bins. Where Cappellari & Copin compute the SNR of a bin by means of

$$SNR = \frac{\sum_i Signal_i}{\sqrt{\sum_i Noise_i}},$$

where $Signal_i$ and $Noise_i$ are precomputed signal and noise value of the spectra that will be binned, the SNR of the spectra presented in this paper have been recomputed each time a new spectrum was added to a bin. In short, each time a spectrum was added, it was summed with the other spectra of the bin and a new SNR was recomputed by means of

$$SNR = \frac{N}{\sqrt{N + \sigma^2}},$$

where σ is the dispersion of the continuum of the spectrum and N the number of photons composing the emission line located above the continuum. Typically, a target SNR of 5 has been used. After the binning process, a Delaunay triangulation algorithm was used to smooth bins of each channel of the data cubes.

This smoothing method has been preferred to the fixed-sized kernel convolution (such as a 6×6 gaussian). Adaptive spatial binning allows the spatial resolution to be kept in high SNR regions while still providing large signal coverage in low SNR regions.

3.4 Radial velocity map extraction

Radial velocity, monochromatic, continuum and dispersion maps are extracted with a single emission line detection algorithm. This algorithm is based on barycenter computation. The central position of the emission line is computed

with photons above the continuum that constitute the emission line. The radial velocity is then computed as

$$v_{obs} = \left(\frac{\left(\frac{\lambda_{obs}}{\lambda_0} \right)^2 - 1}{\left(\frac{\lambda_{obs}}{\lambda_0} \right)^2 + 1} \right) * c + corr,$$

where λ_{obs} is the emission line computed barycenter wavelength, λ_0 the rest wavelength (here, $H\alpha$), c the speed of light in vacuum and $corr$ the heliocentric velocity correction computed for the time of the observation.

In the case where more than one velocity component are present in the spectrum, only the strongest emission line will be taken into account. When two emission lines are spectrally close and have comparable amplitudes, they may be taken as a single one having a larger velocity dispersion. More details are available in Daigle et al. (2006).

3.5 Astrometry

Astrometric information was attached to the processed files by using the task `koords` in the KARMA package (Gooch, 1996). Right ascension, declination, pixel size and field rotation information are embedded in all files and permit their easy comparison with other survey images (DSS, 2MASS, SPITZER). To do so, original ADHOCw files types (ad2, ad3) were modified to allow these data to be stored. This is also an important step since the position angle (PA) of the major axis, whose determination is explained in the next section, is field orientation dependent. Moreover, the astrometric information is necessary to combine the kinematical data to the SINGS and ancillary multi wavelength surveys.

3.6 Kinematical parameters

The ROTCUR routine in the GIPSY package was used to find the kinematical parameters of the galaxies studied. ROTCUR works by fitting tilted ring models to velocity information found in the velocity maps. V_{obs} is obtained using the following equation:

$$V_{obs} = V_{sys} + V_{rot}(R) \cos \theta \sin i + V_{exp}(R) \sin \theta \sin i,$$

where V_{sys} is the systemic velocity of the system studied, V_{rot} is the rotation velocity, V_{exp} the expansion (non-circular) velocity, i the inclination of the ring and R and θ the polar coordinates in the plane of the galaxy. The same procedure was used for all the galaxies of the sample. To allow for a good sampling frequency, the ring width used was always at least 3 times the pixel size.

The extraction of the kinematical parameters is done as follows. The photometrical parameters of the galaxies (position angle (PA), inclination (i)) are taken from the RC3 catalog as initial parameters. The photometrical inclination is calculated as $I = \cos^{-1}(10^{-R_{25}})$. The rough rotational center of the galaxies is taken by looking at the continuum maps extracted at section 3.4 and taking the point where the continuum is the highest near the center of the galaxy (usually obvious for spiral galaxies, trickier for irregular, low surface brightness and distorted ones). The starting point of

Table 5. Photometrical and kinematical parameters

Galaxy name	Photometrical ⁽¹⁾		Kinematical	
	PA(°)	Incl.(°)	PA(°)	Incl.(°)
NGC 628	25	24	26.4 \pm 2.4	21.5 \pm 4.5
NGC 925	102	56	105.0 \pm 1.0	50.0 \pm 1.5
NGC 2403	127	56	125.0 \pm 1.0	60.0 \pm 2.0
NGC 2798	160	68	— ⁽²⁾	— ⁽²⁾
NGC 2915	129	59	— ⁽²⁾	— ⁽²⁾
NGC 2976	323 ⁽³⁾	63	323.5 \pm 3.5	70.2 \pm 4
NGC 3049	25	49	— ⁽²⁾	— ⁽²⁾
NGC 3031	337 ⁽³⁾	58	332.9 \pm 1.2	62.4 \pm 1
UGC 5423	320 ⁽³⁾	49	320.5 \pm 5	58.8 \pm 6
NGC 3184	135	21	176.4 \pm 4 ⁽⁴⁾	16.7 \pm 1.1
NGC 3198	35	67	33.9 \pm 0.3	69.8 \pm 0.8
NGC 3521	343 ⁽³⁾	62	342.0 \pm 1.1	66.7 \pm 2
NGC 3621	339 ⁽³⁾	55	342.5 \pm 2.9	65.2 \pm 4
NGC 3938	151 ⁽³⁾⁽⁵⁾	24	199.5 \pm 5 ⁽⁴⁾	7.7 \pm 3.2
NGC 4236	162	71	156.1 \pm 1.6	76.1 \pm 0.7
NGC 4321	30	32	27.0 \pm 1.0	31.7 \pm 0.7
NGC 4536	310 ⁽³⁾	65	300 \pm 2	68 \pm 3
NGC 4569	23	63	24.7 \pm 4.4	66.7 \pm 5
NGC 4579	95	37	89.5 \pm 4.5	45.7 \pm 7.3
NGC 4625	162 ⁽³⁾⁽⁵⁾	29	126 \pm 5 ⁽⁴⁾	35.9 \pm 6
NGC 4725	35	45	30.3 \pm 1.6	50.8 \pm 2.1
NGC 5055	105	55	98.0 \pm 1.9	63 \pm 2
NGC 5194	163	52	169.0 \pm 4.2	47 \pm 5
NGC 5398	172	53	— ⁽²⁾	— ⁽²⁾
NGC 5713	190 ⁽³⁾	27	203 \pm 5.8	33 \pm 4.8
IC 4710	5	39	— ⁽²⁾	— ⁽²⁾
NGC 6946	250 ⁽³⁾⁽⁵⁾	32	239.0 \pm 1.0	38.4 \pm 3.0
NGC 7331	171	69	165 \pm 1.2	78.1 \pm 2.7

⁽¹⁾Photometrical parameters taken from the RC3 catalog.

⁽²⁾It is useless or impossible to determine the kinematical parameters for this galaxy due either to the lack of large-scale rotation or the interaction with another galaxy.

⁽³⁾A 180° rotation was applied to the photometrical PA in order to be able to compare it with the kinematical PA.

⁽⁴⁾The photometrical and kinematical PA do not agree even with a 180° rotation. This usually happens for face-on galaxies.

⁽⁵⁾This photometrical parameter was not available in the RC3 database and was taken from the 2MASS Large Galaxies Atlas.

the systemic velocity is the one used to select the interference filters, as explained in section 2.2.

The initial photometrical PA must be sometimes corrected ($\pm 180^\circ$) to properly represent the kinematical PA, that is, the angle from North Eastwards to the receding side of the galaxy. Also, GIPSY does not take into account the field rotation of the supplied radial velocity map. The starting PA is adjusted in order to reflect this.

First, ROTCUR is run to find the real kinematical center of the galaxy and its systemic velocity by fixing both PA and i and leaving the other parameters free. The analysis of the output of ROTCUR is made with IDL routines that permit the extraction of statistics on the free parameters, such as median, mean, error weighted mean, standard deviation and linear fit. If the output is too noisy, ROTCUR

was run again, starting with another set of initial parameters, until the median of the absolute residual of the computed model was below 10 km s^{-1} . Then, having properly determined the kinematical center and the systemic velocity, the real kinematical PA and inclination were set as free parameters, fixing all the others. Finally, having found the five kinematical parameters (x_c , y_c , V_{sys} , PA and i), they were fixed and ROTCUR was run again to find V_{rot} . It was decided to use fixed values of PA and i across the whole galaxy as disks are rarely warped inside their optical part. Warps are mainly seen in disks for $R > R_{opt}$. However, the PA is observed to vary as function of radius for some galaxies (e.g. NGC 4579). The PA value is thus chosen in part of the disk where it reaches an almost constant value. The errors on the kinematical parameters found can thus be artificially lowered since the non-axisymmetric parts of the galaxies are discarded from the fit. For barred galaxies, this involved restricting the fit outside the bar. For non-barred galaxies, the outer parts were removed from the fit when the errors were larger than four times the means error.

4 RESULTS

The kinematical parameters found by means of the method described in section 3.6 are presented in table 5.

In Appendix ??, for each galaxy of the sample, the XDSS blue image, the SPITZER $3.6\mu\text{m}$ image, the H α monochromatic image, where the continuum has been suppressed, and the RV map are provided. A Position-Velocity (PV) diagram is given when it was possible to extract the kinematical parameters from the radial velocity map. The red line superposed to the PV diagram is the velocity of the major axis of the galaxy's model reconstructed from its rotation curve. All images for a given galaxy have the same angular scale. Blue, IR and H α monochromatic images have a logarithmic intensity scale. The color scales of the radial velocity maps and the PV diagrams are linear.

Since the calibrations and the observations are most of the time done through different interference filters, the presented monochromatic maps could not be flux calibrated.

The rotation curves, extracted as explained in Section 3.6, are presented in Appendix ??. The errors given for the velocity points are the difference between the approaching and the receding side of the galaxy or the formal error given by rotcur, whichever is the largest. We think that this is a better estimate than using directly the formal error of rotcur since this will take into account possible asymmetries between the two sides of the galaxies.

The rotation curves are available in electronic form at http://www.astro.umontreal.ca/fantom/sings/rotation_curves.htm.

5 DISCUSSION

In this section, we discuss the advantages and limitations of H α kinematical observations using integral field spectroscopy over other kinematical observational methods.

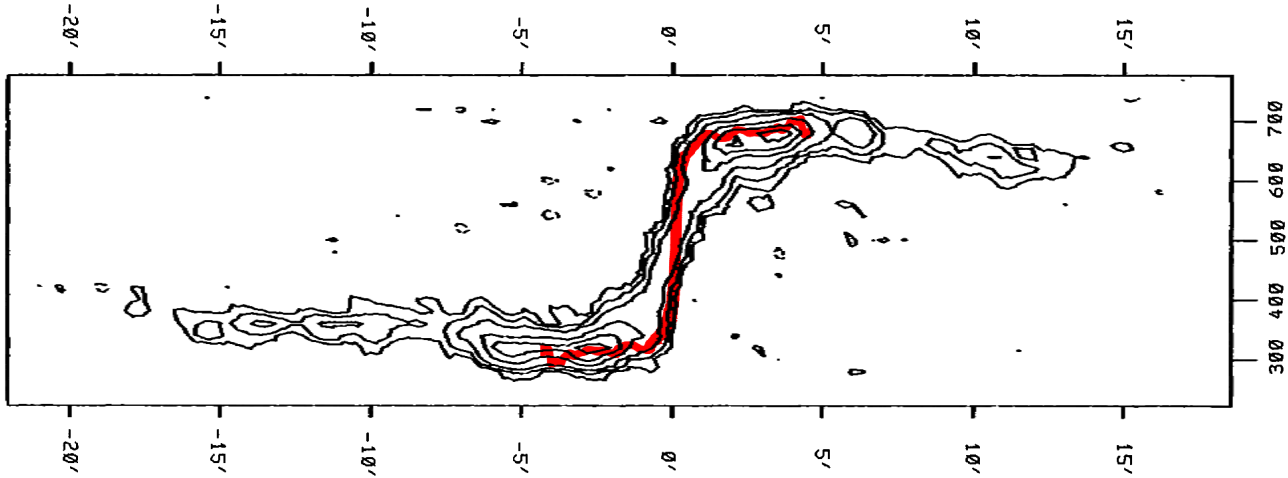


Figure 4. H_I data of NGC 5055 taken from Wevers, van der Kruit, & Allen, 1986, and $H\alpha$ rotation curve superposed on it (red line). This figure clearly shows the effect of beam smearing on H_I data and the need for $H\alpha$ data to resolve the kinematics at the center of galaxies. In H_I , the beam Full Width Half Power (FWHP) was $49'' \times 73''$ while the $H\alpha$ resolution is $1.6'' \times 1.6''$

5.1 Better resolution of the inner rotation curve

Of course, the signal coverage of the $H\alpha$ observations is less extended than for the H_I observations but it allows to resolve the rising part of the rotation curve with greater precision. Figure 4 shows a 21-cm PV diagram of NGC 5055 taken from Wevers, van der Kruit, & Allen (1986). From the 21-cm data alone, one can calculate that the maximum velocity gradient at the center of the galaxy is of the order of $\sim 45 \text{ km s}^{-1} \text{ kpc}^{-1}$. The red line shows the rotation curve derived from the $H\alpha$ data, which has a maximum gradient of $\sim 300 \text{ km s}^{-1} \text{ kpc}^{-1}$. This shows how the 21-cm data are affected by beam smearing. For H_I , the beam Full Width Half Power (FWHP) is $49'' \times 73''$ while the $H\alpha$ resolution is $1.6'' \times 1.6''$.

The rising part of the rotation curve is crucial in the determination of the dark-to-luminous mass ratio (Blais-Ouellette et al., 1999) and in the determination of the mass model parameters. For the sake of comparison, maximum achievable 21-cm beam width at the VLA in B configuration is $\sim 4''$ usable only for the strongest emitting galaxies, while it is $\sim 12.5''$ in C configuration, where sensitivity is high enough to observe the weak galaxies' signal. NGC 5055 harbors double emission lines in its center, as noted by Blais-Ouellette et al. (2004). Resolving such details needs both the high spatial and spectral resolution of the integral field spectroscopy used throughout this study.

5.2 Better determination of the orientation parameters

One of the main advantage of the determination of galaxies' kinematics using integral field spectroscopy at $H\alpha$ over long slit spectroscopy is that there is no *a priori* knowledge needed on the galaxy apart from its systemic velocity (which is usually well known within a $\pm 50 \text{ km s}^{-1}$ range for nearby

galaxies, which is enough for accurate observations). In long slit spectroscopic observations, the PA of the galaxy must be known as the slit must lie on the major axis. The PA is thus usually determined by fitting ellipses to the optical isophotes. As Table 5 shows, there is sometimes a great discrepancy between published photometrical and kinematical parameters.

The effect can be well illustrated with the nearly face-on ($i = 17^\circ$) galaxy NGC 3184. The photometrical PA of 135° is 41° off from the kinematical PA found. This PA error can lead to a substantial underestimate of the rotation velocities for highly inclined galaxies. Also, for some galaxies, the kinematical center is not superposed on the photometrical center. This can also lead to large errors on the rotational velocities.

Figure 5 shows the effect of using the photometrical PA to observe this galaxy in long slit spectroscopy. The resulting rotation curve is less steep in the center of the galaxy and the maximum rotational velocity is underestimated (RMS error is 38.4 km s^{-1}), which affects the mass models used to determine the dark matter content. Using integral field spectroscopy, the kinematical PA is determined *a posteriori* and it does not affect the quality of the data gathered. The figure also presents the residuals of the velocity field models built from the rotation curves extracted. It clearly shows that would the kinematical data have been gathered from long slit observations using the photometrical PA, the results would have been totally erroneous.

On the other hand, it should be considered that the difference between the photometrical and kinematical PA may be partially due to the fact that the photometrical PA would have been more accurately determined by using deep IR images (such as SPITZER images), which shows the old stellar population and is less affected by structural patterns.

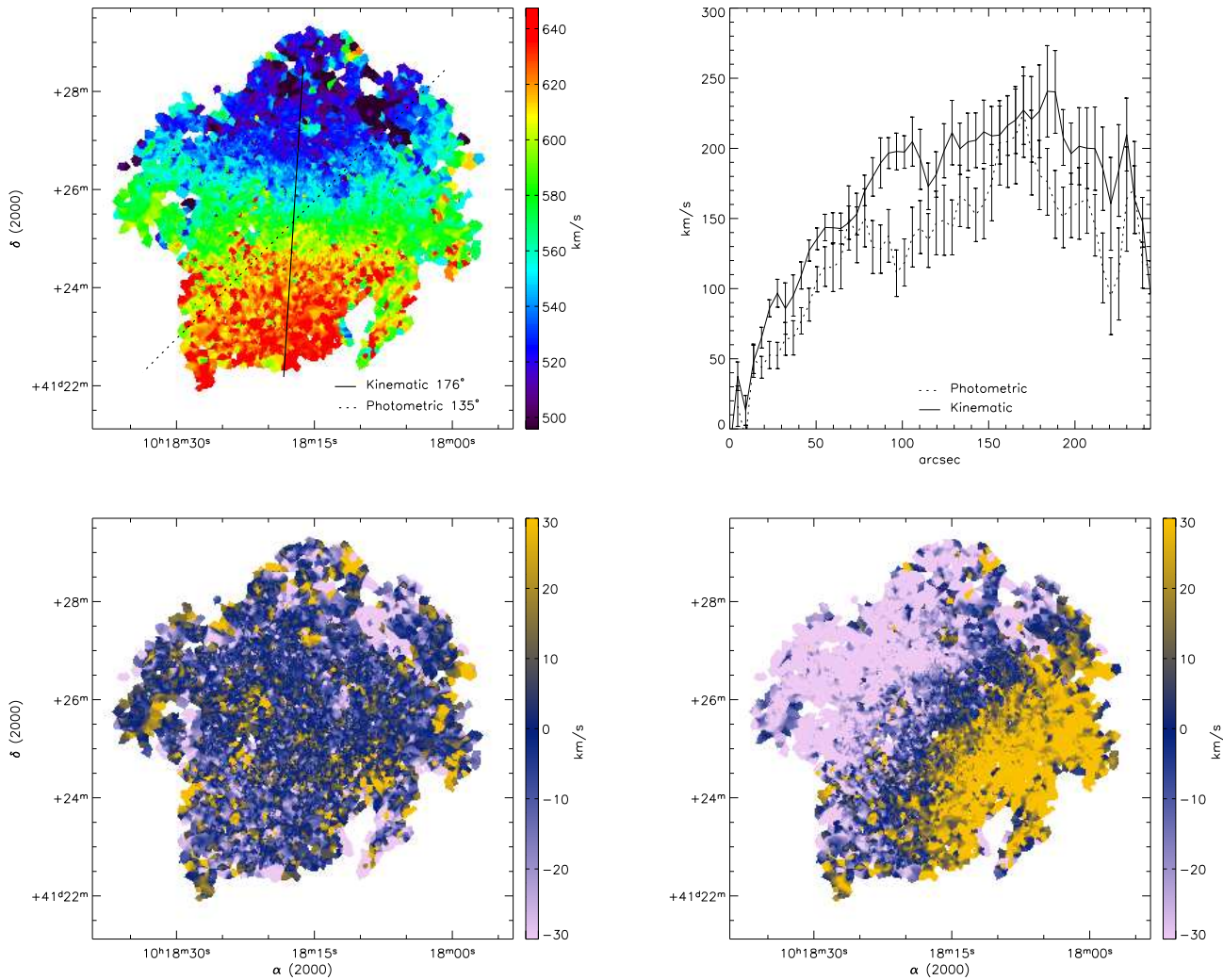


Figure 5. Difference between kinematical and photometrical parameters for NGC 3184. **Top left** : H α velocity field showing kinematical and photometrical PA. **Top right** : Rotation curves extracted from the velocity fields using kinematical and photometrical parameters as if long slit spectroscopy was used for the observations. The RMS error of the photometrical rotation curve is 38.4 km s^{-1} . There is nearly a 30% error around $100''$. **Bottom left** : Residual map of a model built using the kinematical parameters. **Bottom right** : Residual map of a model built using the photometrical parameters.

5.3 Observation of non-axisymmetric motions

Barred galaxies lead to a specific problem since errors on the determination of the PA of the disk can be induced by the bar. For instance, the galaxy NGC 3049 is totally dominated by a bar and its associated non-axisymmetric motions. By taking a look at the blue and IR images of Figure ??, it could be thought, at first, that the PA is somewhere around 20° . However, the isoveLOCITY contours suggest that the PA is more like 60° . This problem is caused by the lack of kinematical information outside the bar dominated region of the galaxy. In this case, H I data would be necessary to resolve the kinematics outside the bar, since the global kinemat-

ical parameters must be extracted from the axisymmetric portion of the galaxy.

This galaxy demonstrates clearly the advantage of 2D velocity fields over 1D long-slit data. 2D velocity fields allow to disentangle circular from radial motions while they would be confused in long slit data. Integral field spectroscopy makes it possible to study more thoroughly non circular motions in galaxies, such as in Hernandez et al. (2005), where an in-depth study of barred galaxies is done.

5.4 Observation of highly inclined galaxies

It has been said that $H\alpha$ could not resolve the kinematics for highly inclined galaxies since the gas cannot be considered optically thin at this wavelength (Goad & Roberts 1981). But, the case of NGC 4236, whose inclination is 76° , shows that as long as the galaxy is not perfectly edge-on, the major axis of the galaxy is visible and the kinematics of the disk can be resolved. Figure 6 shows how the $H\alpha$ and H_I kinematics agree. As opposed to the case of NGC 5055, we can compare the $H\alpha$ kinematics to the H_I kinematics since the inner part of the rotation curve is less shallow. However, since the signal coverage is less extended for $H\alpha$ than it is for H_I , the flat part of the rotation curve is missing from the $H\alpha$ data. Also, as stated by Bosma et al. (1992), as spiral galaxies can be considered optically thin at least for the outer part of the visible disk ($R > 0.5R_{25}$), $H\alpha$ observations can be used to resolve their kinematics.

6 CONCLUSION

The $H\alpha$ kinematics of 28 galaxies of the SINGS survey were presented in this paper. The observations were made with FANTOMM, an integral field FP spectrometer and a photon counting camera. The raw data obtained at the telescope were processed through a new pipeline, an adaptive binning algorithm has been applied to achieve optimal signal-to-noise ratio and the radial velocity maps were finally extracted from the data cubes using a selective intensity weighted mean algorithm. Kinematical parameters were computed using a tilted ring model and most of them agreed within an acceptable error range with the photometrical parameters, except for a few problematic galaxies. It has been shown that high spatial resolution data is essential for mapping the velocity gradient at the centres of galaxies. The advantages of integral field spectroscopy over long slit spectroscopy were also presented.

The aim of this paper is to provide accurate optical kinematical data for the galaxies of the SINGS survey. These data will be used in a forthcoming paper to present rotation curves and mass models of the non-barred galaxies (Nicol et al. in preparation). The data of some of the barred galaxies of the SINGS sample that are also part of the *BH α BAR* survey were used to derive the bar pattern speeds using the Tremaine–Weinberg method (Tremaine & Weinberg 1984) in a paper presented by Hernandez et al. (2005). These data might also be used to allow for some of the galactic star formation models to include kinematical data and thus try to determine what is the exact role of rotation in the star formation processes on a galactic scale.

The $H\alpha$ kinematical data for all the observable SINGS galaxies will be made available to the community as soon as all the galaxies have been observed.

ACKNOWLEDGEMENTS

We thank Jean-Luc Gach, Philippe Ballard, Olivia Garrido, Jacques Boulesteix and Olivier Boissin from the OAMP, for

their help and support at the different stages of this work. Many thanks also to Bernard Malenfant and Ghislain Turcotte, from the OMM, Pierre Martin and the CFHT staff as well as the ESO 3.6-m telescope team who helped us a lot in making the observing runs a success. We also want to thank the anonymous referee for his valuable comments. The FANTOMM project has been carried out by the Laboratoire d'Astrophysique Expérimentale (LAE) of the Université de Montréal using a grant from the Canadian Foundation for Innovation and the Ministère de l'Éducation du Québec. This project made use of the LEDA database: <http://leda.univ-lyon1.fr/>.

REFERENCES

- Arsenault R., Roy J.-R., Boulesteix J. 1990, *A&A*, 234, 23
- Begeman K. G. 1989, *A&A*, 223, 47
- Blais-Ouellette S., Carignan C., Amram P., Côté S., 1999, *AJ*, 118, 2123
- Blais-Ouellette S., Amram P., Carignan C., Swaters R., 2004, *A&A*, 420, 147
- Boselli A., 2001, *ApSSS*, 277, 401
- Bosma A., 1981, *AJ*, 86, 1791
- Bosma A., Byun Y., Freeman K. C., Athanassoula E., 1992, *ApJ*, 400, L21
- Broeils A. H., van Woerden H., 1994, *A&AS*, 107, 129
- Bronkalla W., Notni P., Mutter A. A.-R., 1992, *AN*, 313, 1
- del Burgo C., Laureijs R. J., Ábrahám P., Kiss C., 2003, *MNRAS*, 346, 403
- Buta R., 1995, *ApJS*, 96, 39
- Canzian B. J., 1990, Ph.D. Thesis, California Inst. of Tech., Pasadena.
- Canzian B., Allen R. J. 1997, *ApJ*, 479, 723
- Cappellari M., Copin Y., 2003, *MNRAS*, 342, 345
- Carignan C., Charbonneau P., Boulanger F., Viallefond F. 1990, *A&A*, 234, 43
- Casertano S., van Gorkom J. H., 1991, *AJ*, 101, 1231
- Cayatte V., van Gorkom J. H., Balkowski C., Kotanyi C. 1990, *AJ*, 100, 604
- Cepa J., Beckman J. E. 1990, *A&AS*, 83, 211
- Chemin L., et al., 2006, *MNRAS* accepted, arXiv:astro-ph/0511417
- Conti P. S., 1991, *ApJ*, 377, 115
- Corradi R. L. M., Boulesteix J., Bosma A., Amram P., Capaccioli M. 1991, *A&A*, 244, 27
- Daigle, O., Carignan, C., Hernandez, O., Chemin L., Amram, P., submitted to *MNRAS*
- Elmegreen B. G., Wilcots E., Pisano D. J. 1998, *ApJ*, 494, L37
- Erwin P., 2004, *A&A*, 415, 941
- Fraternali F., Oosterloo T., Sancisi R., van Moorsel G. 2001, *ApJ*, 562, L47
- Gach J.-L., Hernandez, O.; Boulesteix, J.; Amram, P.; Boissin, O.; Carignan, C.; Garrido, O.; Marcelin, M.; Östlin, G.; Plana, H.; Rampazzo, R., 2002, *PASP*, 114, 1043
- Garcia-Burillo S., Sempere M. J., Combes F., Neri R. 1998, *A&A*, 333, 864

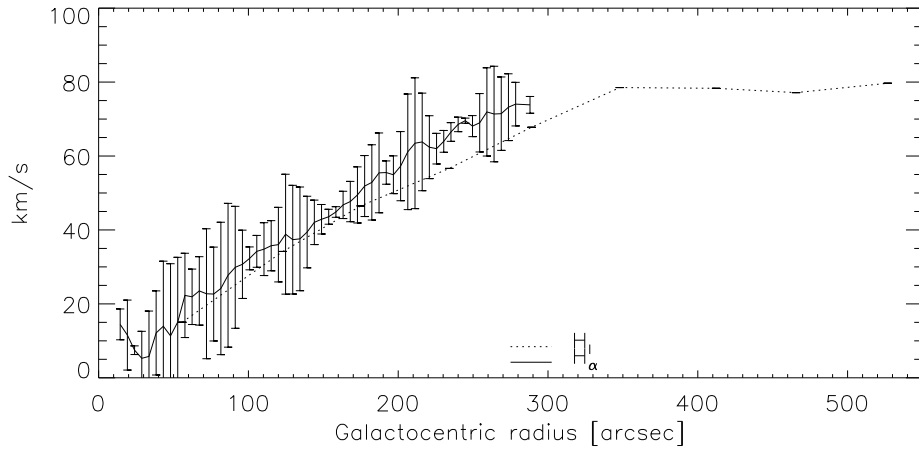


Figure 6. NGC 4236 rotations curves obtained in H α and H I . The H I data are taken from Huchtmeier (1975).

Gil de Paz et al., submitted to ApJ

Goad J. W., Roberts M. S., 1981, ApJ, 250, 79

Gonzalez Delgado R. M., Perez E., 1996, MNRAS, 281, 1105

Gordon K. D., et al., 2004, ApJS, 154, 215

Helfer, T. T., Thornley, M. D., Regan, M. W., Wong, T., Sheth, K., Vogel, S. N., Blitz, L., & Bock, D. C.-J. 2003, ApJS, 145, 259

Hernandez O., Gach J., Carignan C., Boulesteix J., 2003, SPIE, 4841, 1472

Hernandez O., Carignan C., Amram P., Chemin L., Daigle O., 2005, MNRAS, 360, 1201

Hernandez O., Wozniak H., Carignan C., Amram P., Chemin L., Daigle O., 2005, ApJ, 632, 253

Huchtmeier W. K., 1975, A&A, 45, 259

Kamphuis J., Briggs F., 1992, A&A, 253, 335

Kennicutt R. C., 1989, ApJ, 344, 685

Kennicutt R. C., et al., 2003, PASP, 115, 928

Knapen J. H., Cepa J., Beckman J. E., Soledad del Rio M., Pedlar A. 1993, ApJ, 416, 563

Knapen J. H., Shlosman I., Heller C. H., Rand R. J., Beckman J. E., Rozas M. 2000, ApJ, 528, 219

Kuno N., Nakai N., 1997, PASJ, 49, 279

Marcelin M., Boulesteix J., Courtes G. 1982, A&A, 108, 134

Marcelin M., Petrosian A. R., Amram P., Boulesteix J., 1994, A&A, 282, 363

Marquez I., Moles M., 1996, A&AS, 120, 1

Meurer G. R., Carignan C., Beaulieu S. F., Freeman K. C., 1996, AJ, 111, 1551

Nishiyama K., Nakai N., Kuno N., 2001, PASJ, 53, 757

Nordgren T. E., Helou G., Chengalur J. N., Terzian Y., Khachikian E., 1995, ApJS, 99, 461

Pellet A., Simien F., 1982, A&A, 106, 214

Pisano D. J., Wilcots E. M., Elmegreen B. G. 1998, AJ, 115, 975

Pogge R. W., 1989, ApJS, 71, 433

Rand R. J. 1995, AJ, 109, 2444

Regan M. W., et al., 2004, ApJS, 154, 204

Rosenberg J. L., Schneider S. E., 2003, ApJ, 585, 256 .

Rots A. H., Crane P. C., Bosma A., Athanassoula E., van der Hulst J. M., 1990, AJ, 100, 387

Sakamoto K., Okumura S., Minezaki T., Kobayashi Y., Wada K. 1995, AJ, 110, 2075

Sandage A., 1986, ARA&A, 24, 421

Schaap W. E., Sancisi R., Swaters R. A. 2000, A&A, 356, L49

Schoenmakers R. H. M., Franx M., de Zeeuw P. T. 1997, MNRAS, 292, 349

Shostak G. S. 1973, A&A, 24, 411

Sofue Y., Tomita A., Tutui Y., Honma M., Takeda Y. 1998, PASJ, 50, 427

Sofue Y., Koda J., Nakanishi H., Onodera S., Kohno K., Tomita A., Okumura S. K., 2003, PASJ, 55, 17

Stil J. M., Israel F. P., 2002, A&A, 389, 42

Tremaine S., Weinberg M. D., 1984, ApJ, 282, L5

Tosaki T., Shioya Y., 1997, ApJ, 484, 664

van der Kruit P. C., Shostak G. S., 1982, A&A, 105, 351

Vogt N. P., Haynes M. P., Herter T., Giovanelli R. 2004, AJ, 127, 3273

Tilanus R. P. J., Allen R. J., 1991, A&A, 244, 8

Tschöke D., Bomans D. J., Hensler G., Junkes N., 2001, A&A, 380, 40

van Moorsel G. A., 1983, A&AS, 54, 19

Vollmer B., Balkowski C., Cayatte V., van Driel W., Huchtmeier W., 2004, A&A, 419, 35

Wevers B. M. H. R., van der Kruit P. C., Allen R. J., 1986, A&AS, 66, 505

Willner S. P., et al., 2004, ApJS, 154, 222

Young J. S., et al., 1995, ApJS, 98, 219

APPENDIX A: DESCRIPTION OF THE INDIVIDUAL GALAXIES

A brief description of the structures observed in the H α velocity fields, monochromatic images and PV diagrams of the SINGS sample is made in this appendix. The galaxies NGC 0925, NGC 2403, NGC 3198, NGC 4236, NGC 4321 and NGC 6964 are part of the *BH α BAR* survey and are extensively described in Hernandez et al. (2005). The galaxies NGC 4321, NGC 4536, NGC 4569 and NGC 4579 are part of the sample of 30 Virgo cluster galaxies and will be studied in Chemin et al. (2006).

NGC 628 (M74): The H $_I$ PA of this face-on galaxy varies greatly with distance from the center, as observed by Kamphuis & Briggs (1992). In the visible, this phenomenon is seen in the outer rings of the H α RV map. Some H $_{II}$ regions with velocities that are perpendicular to the plane of the galaxy are also visible. The H $_I$ PA determined by Kamphuis & Briggs (1992) agrees with the kinematical one (Table 5), but the inclination differs greatly (6.5° for H $_I$ and 21.5° for H α). This may be due to the fact that *rotcur* has problems dealing with galaxies whose inclination is $<40^\circ$ (Begeman 1989, Chemin et al. 2006). For the rotation curve presented in Figure ??, the H $_I$ inclination was adopted. This galaxy has also been observed in CO by Nishiyama, Nakai, & Kuno (2001).

NGC 925: This late type SBcd galaxy has a bright optical and H α bar and two bright patchy spiral arms beginning at the ends of the bar. Many H $_{II}$ regions lie along the bar. The photometrical and kinematical data agree. The PV diagram shows non axisymmetric motions near the center. It is well studied in H $_I$ (Elmegreen, Wilcots, & Pisano 1998; Pisano, Wilcots, & Elmegreen 1998), in CO (Helfer et al. 2003) and in H α (Marcelin, Boulesteix, & Courtes 1982). It shows strong streaming motions.

NGC 2403: This SABc galaxy shows amorphous spiral features. The H α velocity maps and the PV diagram show an almost rigid structure near the center of the galaxy. Bright H $_{II}$ regions can be seen in the H α monochromatic image. It is not clear whether this galaxy is barred or not. According to Schoenmakers, Franx, & de Zeeuw (1997), their Fourier harmonic analysis of the H $_I$ velocity field shows that non-circular motions are not important in this galaxy. Moreover, Schaap, Sancisi, & Swaters (2000) stress that the thin hydrogen disk of NGC 2403 is surrounded by a vertically extended layer of H $_I$ that rotates slower than the disk. A complete modeling of the galaxy will provide more details on its structures. Fraternali et al. (2001) suggest that this anomalous H $_I$ component may be similar to a class of high velocity clouds observed in the Milky Way. In CO data, no molecular gas is detected (Helfer et al. 2003).

NGC 2798: This galaxy is interacting with its close companion, NGC 2799 on the east. Marquez & Moles (1996) observed a difference of 125 km s^{-1} in the velocity of the H $_I$ and H $_{II}$ components of NGC 2799. Due to this interaction, it was useless to determine the kinematical parameters of this galaxy (Table 5).

NGC 2915: The radial velocity map of this galaxy

shows a highly distorted optical disk. This renders impossible the determination of the kinematical parameters of the galaxy. Two bright H $_{II}$ regions are visible toward the center of the galaxy. Meurer et al. (1996) obtained the H $_I$ kinematics of this blue compact dwarf galaxy. They observed that the optical disk of the galaxy corresponds to the central H $_I$ bar. They think that the dark matter halo dominates at nearly all radii.

NGC 2976: This peculiar dwarf late type galaxy has a nearly linear rotation curve. There is no spiral arm visible. Two strong H $_{II}$ regions are located on each side of the galaxy. Stil & Israel (2002) observed that in H $_I$ the rotation curve seems to flatten near the edge of the H $_I$ disk. According to Bronkalla, Notni, & Mutter (1992), the outer parts of NGC 2976 have been undisturbed for a long time and are very old (5 Gy, probably up to 15 Gy).

NGC 3031 (M81): The great M81 spiral galaxy has few H α emission in its center, given its somewhat early type (Sab). The velocity information for radii up to $\sim 4'$ is thus difficult to extract. Farther away from the center, the rotation curve is very flat and does not show any decrease near the edge of the optical disk. Long slit observations performed by Pellet & Simien (1982) show the same flattening. The bright core, as seen in infrared, contrasts greatly with its dim H α counterpart. Detailed investigation of the UV, H α and IR SFR indicators based on SPITZER and SINGS ancillary data have been done by Gordon et al. (2004) and suggests that the central dust is heated by stars in the bulge rather than star formation. The morphological analysis of the IR data that has been done by Willner et al. (2004) and shows evolved stars organized in bulge and disk components, a dusty interstellar medium showing star forming regions and a clumpy profile. Still according to Willner et al., the flux density of the pointlike nucleus seems to have decreased by a factor of three in the past four years.

NGC 3049: This Makarian galaxy harbours a “double nucleus”, as stated by Nordgren et al. (1995). This feature, invisible in infrared, is easily seen in H α and it does not seem to affect the galaxy’s kinematics. The “second nucleus” is most probably just a strong starburst H $_{II}$ region. Still according to Nordgen, this galaxy does not show any trace of merging. The galaxy is totally dominated by a bar and the signal is too weak outside the bar to resolve the kinematics, rendering the extraction of kinematical parameters impossible.

UGC 5423 (M81 dwarf B): We present the first available kinematical data for this dwarf galaxy. Rotation is weak.

NGC 3184: CO kinematics have been obtained by Nishiyama, Nakai, & Kuno (2001) for this nearly face-on galaxy. H α data show a pretty flat rotation curve that nearly reaches a flat part within the optical disk.

NGC 3198: This SB(rs)c galaxy has been extensively studied in H $_I$ (Bosma 1981; Begeman 1989), FP H α (Corradi et al. 1991, Blais-Ouellette et al. 1999) and H α and [NII] long-slit spectroscopy (Sofue et al. 1998, Vogt et al. 2004). According to the PV diagram, non circular motions

near the centre can be seen. A strong velocity gradient is also seen perpendicular to the bar major axis.

NGC 3521: The declining H_I rotation curve of this galaxy allowed Casertano & van Gorkom (1991) to call for the end of the “disk-halo conspiracy”. Though not visible in H α , the rotation curve starts to decline within a radius of 22 kpc and the H α data stops at 13 kpc.

NGC 3621: Many strong H_{II} regions are visible in this galaxy at all galactic radii. The H α data do not seem to reach the flat part of the rotation curve. This galaxy has been observed by using three fields of the ESO/La Silla 3.6-m telescope. More kinematical data could be gathered by observing further north and south of the galaxy.

NGC 3938: The nearly face-on orientation of this galaxy allowed van der Kruit & Shostak (1982) to study it in H_I to search for extra-planar velocity components. An in-depth study of the H α velocity map is required in order to corroborate this.

NGC 4236: This late type SBdm galaxy is seen nearly edge-on. Its kinematical inclination is 76°. The H α image shows that the H_{II} regions are distributed along the bar, with two bright regions near the end of the bar. These features are also seen in H_I (Shostak 1973). An extensive region of solid-body rotation coincides with the bar.

NGC 4321 (M100): This grand-design spiral galaxy is located in the Virgo Cluster. It has been frequently mapped in the H α emission line using high-resolution FP interferometry (Arsenault, Roy, & Boulesteix 1990, Cepa & Beckman 1990, Canzian & Allen 1997, Knapen et al. 2000), in the molecular CO emission-line (Canzian 1990, Sakamoto et al. 1995, Rand 1995, Garcia-Burillo et al. 1998, Helfer et al. 2003) and in the 21-cm H_I emission-line (Cayatte et al. 1990, Knapen et al. 1993). The H_I disk is almost totally confined within the optical one but with a slight lopsidedness towards the SW (Knapen et al. 1993). The H_I, CO and H α velocity fields show kinematical disturbances such as streaming motions along the spiral arms and a central S-shape distortion of the iso-velocity contours along the bar axis. The circum-nuclear region shows the presence of an enhanced star formation region as a four-armed H α ring-like structure and a CO & H α spiral-like structure. Much more details can be found in Hernandez et al. (2005) and in Chemin et al. (2006).

NGC 4536: Streaming motions along the spiral arms and a Z-shape of the velocities in the central parts are observed in this barred galaxy. As in the CO data (Sofue et al., 2003), a steep velocity gradient is observed in the H α data.

NGC 4625: This galaxy has a close companion, lying 8' away, which is only 22 kpc distant. The galaxy has a very weak rotation and harbours a lot of double profile emission lines, a sign of non-circular activity. This explains the large errors on the kinematical parameters found and the “boiling” aspect of the H α velocity field extracted. van Moorsel (1983) studied it in H_I and found a neutral hydrogen disk having a diameter of 5', which is ~ 5 times larger than the observed H α disk. GALEX images of this galaxy show a very extended UV disk, extending at least 2–3 times the radius of the main star-forming disk (Gil de Paz et al. 2005).

NGC 4569 (M90): This galaxy is located in the Virgo cluster. An off-plane structure to the West of the disk of NGC 4569 has been seen through deep H α imaging (Tschöke et al., 2001) and in H_I data (Vollmer et al., 2004). It is observed here as a string of H_{II} regions whose kinematics follows the rotation of the disk, although it is slightly more red-shifted than inside the disk at equal azimuth angles (Chemin et al. 2006).

NGC 4579 (M58): In addition to the main large-scale spiral arms, this Virgo galaxy exhibits a nuclear spiral structure (the so-called “loop” in Pogge, 1989 and Gonzalez Delgado & Perez, 1996) within which is detected a gradient of up to $\sim 500 \text{ km s}^{-1}$. The FP velocity field shows that the kinematical PA of this nuclear spiral differs by $\sim 90^\circ$ from that of the main spiral arms. The kinematical parameters of this galaxy shown in Table 5 are calculated for the grand-design spiral structure (ie. outside of the nuclear spiral structure). See Figure ?? . The PA of the nuclear structure is $\simeq 174^\circ \pm 11$ (Chemin et al. 2006).

NGC 4725: This barred ringed Sab lenticular galaxy is catalogued as a double barred galaxy by Erwin (2004) and H_I rich by Rosenberg & Schneider (2003). No kinematical data are available for this galaxy. The kinematics in the center of the galaxy are hard to resolve given its early type.

NGC 5055 (M63): This galaxy shows several arm patterns that are well visible in H α . It harbours a very strong velocity gradient in its center and a flat rotation curve. No bar structure is visible. It has been studied in H_I by Bosma (1981) and in CO by Nishiyama, Nakai, & Kuno (2001). This galaxy has also been studied in H α by Blais-Ouellette et al. (2004), which showed two velocity components in its central region. The H α images presented in this paper have weaker response on the receding side of the galaxy than on the approaching side due to the wide span in the galaxy's velocities which made the receding emission fall on the wing of the interference filter.

NGC 5194 (M51a): Two emission lines are visible in the very center of the galaxy and may account for the “dip” in the rotation curve shown in the PV diagram. The strong H_{II} regions discriminate the great spiral structure from the rest of the galaxy. A flow of H_{II} regions is seen extending towards its companion. This galaxy has been studied in H_I by Rots et al. (1990), in both H_I and H α (scanning FP) by Tilanus & Allen (1991) and more recently in CO by Kuno & Nakai (1997). NGC 5195, the galaxy's companion, has been observed in H α through this study but it is impossible to get kinematical information as it is an early type galaxy (SB0p).

NGC 5398: This study provides the first kinematical data for this galaxy. Its peculiar radial velocity map makes it impossible to extract kinematical parameters. It has been classified as ringed galaxy by Buta (1995) and Wolf-Rayet galaxy by Conti (1991).

NGC 5713: Many strong H_{II} regions are visible in this galaxy and produces a oddly looking radial velocity map. There were no kinematical data available for this galaxy prior to publishing this paper.

IC 4710 : This galaxy has plenty of H_{II} regions but does not seem to harbour large-scale rotation.

NGC 6946: According to H_I studies (Carignan et al. 1990), the H_I distribution is not symmetric but is more extended to the NE side. This feature is also seen in the H α emission map. The overall H α velocity map is regular but shows some non-circular motions near the center, confirmed by the PV diagram. It has been recently observed in FP by Blais-Ouellette et al. (2004) leading to the same conclusions. Once again the wide field of FANTOMM and its high sensitivity is clearly an advantage to obtain better H α velocity fields. CO data has been gathered by Young et al. (1995).

NGC 7331: The receding part of the galaxy is invisible in the RV maps presented in this paper. It was first thought that this part of the galaxy was out of the interference filter, but this feature has also been observed by Marcelin et al. (1994). An *a posteriori* scan of the interference filter used showed that the galaxy should have been well centered in the filter. Deep H α images taken by Regan et al. (2004) at the KPNO 2.1 meter telescope show the same asymmetric emission pattern. However, Regan et al. (2004) also made Pa α observations and did not observe that asymmetry. A theory to explain this is that a ring of dust located south of the center of the galaxy is blocking the H α emission from reaching us whilst letting the Pa α through. This galaxy has been called “Post starburst” by Tosaki & Shioya (1997) who studied its kinematics in CO. CO data have also been gathered by Nishiyama, Nakai, & Kuno (2001).

APPENDIX B: OBSERVATIONAL DATA

Figures were removed for the astro-ph version of this paper due to file size constraints. You can access them online at <http://www.astro.umontreal.ca/fantommm/sings>.

APPENDIX C: ROTATION CURVES

Figures were removed for the astro-ph version of this paper due to file size constraints. You can access them online at <http://www.astro.umontreal.ca/fantommm/sings>. The rotation curves in their electronic form are available at http://www.astro.umontreal.ca/fantommm/sings/rotation_curves.htm.

This paper has been typeset from a T_EX/ L^AT_EX file prepared by the author.